



International Journal of Information and Communication Technology

ISSN online: 1741-8070 - ISSN print: 1466-6642

<https://www.inderscience.com/ijict>

Multi-scale adaptive graph convolution-based thick cloud removal method for optical remote sensing images

Honghua Qiu, Kaili Zhang

DOI: [10.1504/IJICT.2025.10071097](https://doi.org/10.1504/IJICT.2025.10071097)

Article History:

Received:	10 March 2025
Last revised:	28 March 2025
Accepted:	28 March 2025
Published online:	27 May 2025

Multi-scale adaptive graph convolution-based thick cloud removal method for optical remote sensing images

Honghua Qiu*

School of Applied Technology,
Zhumadian Preschool Education College,
Zhumadian, Henan,
463000, China
Email: 10271@zyz.edu.cn

*Corresponding author

Kaili Zhang

Henan Institute of Surveying and Mapping,
Zhengzhou, Henan,
450003, China
Email: 18737167540@163.com

Abstract: Cloud occlusion challenges remote sensing image processing by degrading quality and analysis accuracy. Existing cloud removal methods capture local features but struggle with global dependencies and cloud morphology, limiting detail restoration and consistency. To address this, we propose a multi-scale adaptive graph convolution generative adversarial network (MAGC-GAN), integrating a multi-scale adaptive graph convolution network (MAGCN) and an adaptive patch discriminator (APD). MAGCN enhances spatial dependencies using adaptive graph convolution, effectively reconstructing cloud-covered regions by capturing global contextual relationships. A multi-scale feature fusion mechanism enables adaptation to varying cloud thicknesses. APD improves fine-detail recovery by evaluating multiple local patches individually, using an adaptive affine transformation matrix. It also incorporates texture-aware and global consistency losses to restore high-frequency details while maintaining coherence. Compared to existing methods, MAGC-GAN significantly enhances cloud-occluded region restoration, particularly in detail recovery and precise cloud edge reconstruction.

Keywords: remote sensing image; cloud removal; graph convolutional network; GCN; generative adversarial network; GAN; adaptive.

Reference to this paper should be made as follows: Qiu, H. and Zhang, K. (2025) 'Multi-scale adaptive graph convolution-based thick cloud removal method for optical remote sensing images', *Int. J. Information and Communication Technology*, Vol. 26, No. 15, pp.57–77.

Biographical notes: Honghua Qiu graduated from Henan Institute of Education University in 1997 (currently Henan Finance University). He worked in Zhumadian Preschool Education College. His research interest includes optics.

Kaili Zhang graduated from China University of Geosciences (Wuhan), majoring in engineering management. She graduated in 2013 with a Bachelor's degree in Management. At present, she works as an Engineer in Henan Provincial Institute of Surveying and Mapping, and her research field is surveying and mapping.

1 Introduction

Remote sensing imagery has wide-ranging applications in geographic information systems, environmental monitoring, disaster assessment, and other fields (Zhou et al., 2024a; Ebel et al., 2023; Ji and Zhong, 2024). However, cloud occlusion remains a significant challenge that affects both image quality and analytical accuracy (Zhao and Jia, 2023; Zheng et al., 2023; Jing et al., 2023). Clouds not only obscure ground objects, leading to data loss, but also interfere with subsequent image analysis and pattern recognition tasks. In cases of thick cloud coverage, cloud removal becomes particularly difficult, as it involves complex image restoration and detail reconstruction (Liu et al., 2023a; Li et al., 2023b; Zhao et al., 2023). Traditional cloud removal methods primarily rely on pixel-based techniques, filtering approaches, or physical models. However, these methods exhibit limitations in handling the complex morphology of clouds, restoring fine details, and maintaining global consistency in the reconstructed images (Liu et al., 2024b; Dou et al., 2024; Zhou et al., 2022). In recent years, deep learning, particularly generative adversarial networks (GANs) and convolutional neural networks (CNNs), has emerged as a promising solution for cloud removal tasks (Jin et al., 2024; Zhou et al., 2024b; Ma et al., 2025; Han et al., 2024).

Existing cloud removal methods can be broadly classified into traditional image processing-based approaches and deep learning-based approaches. Traditional methods primarily rely on image segmentation (Wang et al., 2024a), filtering (Liu et al., 2023b), and multispectral information fusion (Li et al., 2024a) to identify and remove cloud cover. While effective for simple cloud occlusion scenarios, these techniques struggle to handle the complex nature of cloud interference. On the other hand, deep learning methods, including CNNs (Ma et al., 2023; Zi et al., 2023) and GANs (Zhang et al., 2023; Li et al., 2023a), have shown superior performance in cloud removal by learning image feature representations automatically and leveraging multi-level feature extraction. However, despite their advantages in restoring local details, these methods face two major challenges:

- 1 Due to the limited receptive field of CNNs, they struggle to model global spatial dependencies between pixels, making it difficult to reconstruct complex cloud structures accurately.
- 2 GAN-based methods, while excelling in global image generation, often fall short in restoring fine details and ensuring global consistency, particularly in heavily cloud-covered regions (Hao et al., 2023).

To overcome these limitations, this paper proposes a multi-scale adaptive graph convolution generative adversarial network (MAGC-GAN), which integrates a multi-scale adaptive graph convolution network (MAGCN) and an adaptive patch

discriminator (APD). The core strength of MAGCN lies in its adaptive graph convolution mechanism, which significantly enhances global spatial dependencies among pixels, overcoming the limitation of traditional CNNs that rely solely on local convolution for feature extraction. Compared to existing GCN methods, MAGCN introduces two key breakthroughs. First, conventional GCNs typically construct graphs based on static or predefined adjacency matrices, making it difficult to dynamically adapt to the complex and variable spatial structures within images. In contrast, MAGCN incorporates an adaptive weighting mechanism that automatically adjusts adjacency relationships based on image content, enabling more accurate modelling of pixel-level spatial dependencies. This mechanism not only builds the graph structure according to pixel similarity but also integrates cloud-edge awareness, empowering the network with stronger perceptual and structural understanding in cloud-covered regions. Second, MAGCN integrates multi-scale feature extraction and weighted fusion, greatly improving its adaptability to cloud layers of varying thickness and distribution. Traditional GCNs often construct graphs at a single scale, which limits their ability to simultaneously capture fine-grained local features and broader structural context. MAGCN addresses this by constructing graph convolution branches at multiple scales and fusing the extracted features through adaptive weighting, allowing the network to achieve a better balance between fine detail restoration and global consistency. The APD is introduced to address the shortcomings of traditional discriminators in detail restoration. Conventional GANs use a global discriminator that evaluates the entire image for authenticity. However, this approach often neglects local details, leading to overly smooth or distorted regions in the generated images. APD generates multiple local patches through an adaptive affine transformation matrix and evaluates the authenticity of each patch separately. By independently assessing the realism of each local patch, APD ensures more refined and accurate detail restoration. This design significantly enhances the restoration of fine details, preventing the detail loss commonly seen in traditional methods. Furthermore, APD integrates texture-aware loss and global consistency loss, guiding the generator to restore high-frequency details in cloud-covered areas while ensuring consistency between local details and overall image structure.

The primary contributions of this paper are as follows:

- 1 Proposing the MAGCN, which enhances the global spatial dependencies between pixels through adaptive graph convolution operations. By integrating a multi-scale feature fusion mechanism, it improves the modelling capability of cloud-covered regions, overcoming the limitations of traditional CNNs in global modelling.
- 2 Proposing the APD, which generates multiple local patches and evaluates their authenticity, enhancing local detail recovery and solving the problem where traditional discriminators fail to restore fine details accurately.
- 3 Proposing a GAN combining MAGCN and APD, significantly improving cloud removal performance, particularly in handling complex cloud occlusion and detail recovery, providing an effective solution.

2 Related work

2.1 GAN-based cloud removal

GANs have demonstrated significant potential in cloud removal tasks for remote sensing images. Compared to traditional CNNs, GANs can better model global information and handle the complex structures of clouds. Dou et al. (2024) proposed a cloud removal method based on multi-scale spatial information perception. By employing convolutional kernels of various scales and integrating global semantic and local detail information, the method utilises an attention mechanism to dynamically adjust channel weights, enhancing feature reconstruction performance. However, despite its effectiveness in local detail restoration, this method still falls short in global modelling of cloud structures. Baskar et al. (2024) introduced an unsupervised cloud removal approach that incorporates variational mode decomposition (VMD) to enhance key image information. The method extracts high-information-content regions using VMD and then employs UVCGAN to generate images with thin clouds removed, significantly improving cloud removal effectiveness, particularly in the case of thin cloud occlusion. To address more complex cloud structures, Bie and Su (2024) proposed a multi-scale context-guided feature enhancement cloud removal network (MCGFE-CR). This method utilises a multi-scale context attention-guided module and a residual channel attention module to enhance the fusion of global and local information, thereby improving the quality of cloud removal. Similarly, Xiao (2024) proposed a thin cloud removal method based on multi-scale feature fusion, designed to enhance the network's ability to extract details, achieving excellent results in fine detail restoration. Although these methods have achieved promising results in removing thin clouds, their effectiveness in handling thick clouds remains limited. To address this challenge, Li et al. (2024b) proposed a unified framework for processing both thin and thick clouds. Their method employs a residual structured network to restore image information in thin cloud regions, while leveraging synthetic aperture radar (SAR) images to assist in thick cloud removal. This approach significantly enhances cloud removal quality and visual consistency, achieving remarkable progress, particularly in the restoration of thick cloud-covered areas.

2.2 GCN in remote sensing images

Graph convolutional networks (GCNs) have increasingly demonstrated their unique advantages in remote sensing image analysis, particularly in handling spatial structures and contextual information. Compared to traditional methods, GCNs exhibit superior performance in these aspects. Wang et al. (2024b) proposed a change detection network (CF-GCN), which constructs a coordinate-space graph convolutional network (GCN_C) and a feature-interaction graph convolutional network (GCN_F) in the encoder and decoder, respectively. This approach successfully models spatial relationships and feature interactions within the image, enhancing the perception of image boundaries. Their results indicate that GCNs offer significant advantages in transmitting and precisely extracting boundary information. Zhang et al. (2024) proposed a U-GCN-based method for mining area extraction. By leveraging graph structure propagation and multi-level feature aggregation, the method effectively captures global spatial relationships and contextual information. This demonstrates the potential of GCNs in handling complex spatial structures and multi-level feature information in remote sensing images,

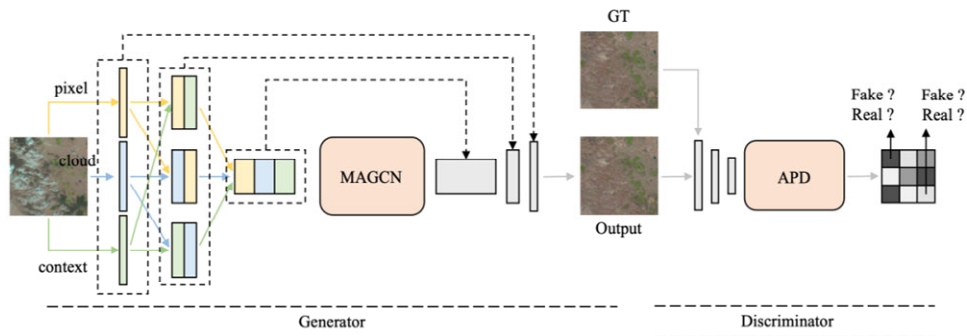
particularly for high-precision target extraction. Lu et al. (2024) introduced the BI2Net method, which employs graph convolution and soft clustering techniques to effectively extract boundary information of target areas. Additionally, their graph interaction module (GIM) enhances the correlation between boundary and internal information. This method highlights the advantages of GCNs in processing image boundaries and complex structures, especially in dynamic and intricate scenes. Song et al. (2024) developed the CSAGC method, which integrates CNN and GCN by designing multiple enhancement modules to process contextual information in remote sensing images. By fusing local and global features, this approach improves change detection performance, demonstrating the strong capability of GCNs in multi-scale spatial information fusion. Liu et al. (2024a) proposed the RDPGNet method, which utilises GCNs for automatic road extraction. Their approach adopts a multi-view information fusion strategy, enhancing the network’s ability to perceive complex road structures. This method showcases how GCNs can effectively handle diverse spatial relationships and adapt to remote sensing images with intricate features.

Although the aforementioned methods are not specifically designed for cloud removal tasks, they highlight the significant advantages of GCNs in processing spatial structures, global information, and boundary perception in remote sensing images. These advantages provide valuable insights for cloud removal, suggesting that GCNs can play a crucial role in modelling relationships between clouds and ground information, as well as improving the accuracy of cloud boundary extraction.

3 Proposed method

To ensure detail restoration and address the issue of global consistency, we propose a MAGC-GAN. The workflow of MAGC-GAN is illustrated in Figure 1.

Figure 1 Workflow of the proposed MAGC-GAN (see online version for colours)



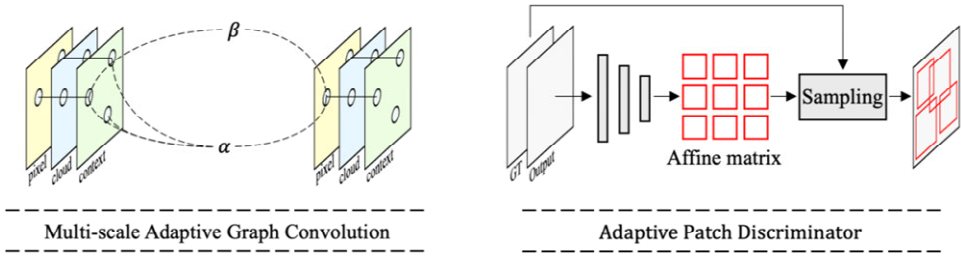
This method is based on a GAN and achieves thick cloud removal through an encoder-decoder structure. The GAN encoder consists of three branches and three stages. In the first branch, the pixel-level features of the input image H_{pixel} are extracted. In the second branch, the cloud structure information H_{cloud} is extracted, describing the cloud’s distribution, occlusion intensity, and hierarchical structure. In the third branch, the contextual information $H_{context}$ is extracted, providing environmental features surrounding

each pixel. After feature extraction, the first stage merges the pixel-level features and cloud structure information to form the first-round fusion features $H_{fusion1} = [H_{pixel}, H_{cloud}]$. The second stage concatenates this fusion feature with the contextual information to obtain the final input feature matrix $H_{input} = [H_{fusion1}, H_{context}]$. This is then fed into the MAGCN for further processing, where MAGCN enhances the global spatial dependencies of the image through graph convolution operations, particularly focusing on structured feature extraction in cloud-covered regions. Next, the decoder restores the image and generates the cloud-removed image $I_{generated}$. This image, along with the real cloud-free image (ground truth), is input into the discriminator for comparison. Furthermore, the generated image $I_{generated}$ is passed through the APD, which evaluates the authenticity of the generated image at multiple granular scales. This guides the network to optimise the generated results, ensuring that the generated image performs well in detail restoration and structural consistency.

3.1 Multi-scale adaptive graph convolution

In the task of thick cloud removal in remote sensing images, the complexity and diversity of cloud occlusion pose challenges for traditional CNNs in handling global dependencies and cloud details. To overcome this issue, this paper proposes a MAGCN, which enhances the network's global modelling capability by integrating adaptive graph convolution operations, multi-scale feature fusion, and cloud structure modelling. The workflow of MAGCN is illustrated in Figure 2.

Figure 2 Workflow of the MAGCN and APD (see online version for colours)



The process of MAGCN is shown in equation (1):

$$H^{(l+1)} = \sigma \left(\sum_{i \in N_j} \alpha_{ij} H_i^{(l)} W^{(l)} + \beta_j H_j^{(l)} \right) \quad (1)$$

where $H^{(l)}$ represents the node feature matrix at layer l , with each node corresponding to a pixel in the image, and the feature vector containing information such as colour and texture. $W^{(l)}$ is the learnable weight matrix of the layer, σ denotes the ReLU activation function, and N_j represents the neighbourhood of node j , which is the set of pixels adjacent to pixel j in the image. To better model the global spatial dependencies of the image, particularly the complex structures in cloud-covered regions, we further introduce the adaptive weight α_{ij} , which dynamically adjusts the adjacency matrix to reflect the spatial dependencies between nodes. Its calculation is given in equation (2):

$$\alpha_{ij} = \frac{e^{-\frac{\|x_i - x_j\|^2}{\sigma^2}}}{\sum_{k \in N_j} e^{-\frac{\|x_j - x_k\|^2}{\sigma^2}}} \cdot (1 + \|\nabla x_i - \nabla x_j\|_2) \quad (2)$$

where $\|x_i - x_j\|^2$ represents the Euclidean distance between nodes i and j , which measures the spatial similarity between pixels. σ controls the attenuation range of similarity, determining the influence of neighbouring pixels. $\|\nabla x_i - \nabla x_j\|_2$ is the edge-aware function, designed to enhance feature extraction in cloud edges or complex structural regions. The adaptive weighting mechanism increases the weight of cloud edges, enabling the network to focus more on feature extraction in complex structural regions, thereby improving cloud removal performance.

Additionally, MAGCN employs a multi-scale feature fusion mechanism to enhance the network's adaptability to multi-scale variations of clouds. Specifically, the feature matrix $H_s^{(l)}$ at each layer is extracted at different scales and, after weighting, forms the final feature matrix. The calculation process is given in equation (3):

$$H_{multi-scale}^{(l)} = \sum_{s=1}^S w_s \cdot H_s^{(l)} \quad (3)$$

where $H_s^{(l)}$ represents the feature matrix extracted at scale s in layer l , w_s denotes the weighting coefficient for each scale, indicating the contribution of different scale features to the final result, and S is the total number of scales. By weighting and fusing features from multiple scales, MAGCN can adapt to clouds of varying thickness and complex occlusion, enabling the network to capture richer feature information at multiple scales and thereby improving the performance of thick cloud removal.

In the design of input features, MAGCN integrates multiple information sources to optimise the construction of the input feature matrix $H^{(l)}$. Specifically, the input feature matrix consists of three components: pixel-level features $H_{pixel}^{(l)}$, cloud structure information $H_{cloud}^{(l)}$, and contextual information $H_{context}^{(l)}$, as shown in equation (4):

$$H^{(l)} = [H_{pixel}^{(l)}, H_{cloud}^{(l)}, H_{context}^{(l)}] \quad (4)$$

where $H_{pixel}^{(l)}$ captures the detailed information of the image, primarily including low-level features such as colour and texture. $H_{cloud}^{(l)}$ describes the distribution, occlusion intensity, and hierarchical structure of clouds, enhancing the modelling capability of cloud-covered regions. $H_{context}^{(l)}$ provides environmental information surrounding each pixel, aiding in the understanding of long-range dependencies, especially in regions with complex cloud occlusion. By integrating these multi-source information components, MAGCN can more comprehensively model the spatial and contextual structure of the image, significantly improving the effectiveness of thick cloud removal.

3.2 Adaptive patch discriminator

To enhance the quality of the generated images and improve detail restoration, we propose a novel discriminator network, the APD. The workflow of APD is illustrated in Figure 2. This method integrates CNNs with adaptive affine transformation matrices to generate multiple local patches and evaluate the authenticity of each patch.

Specifically, given an input image $I \in \mathbb{R}^{H \times W \times C}$, where H and W represent the height and width of the image, respectively, and C denotes the number of channels, the discriminator first extracts global features using a CNN, obtaining a feature map $F \in \mathbb{R}^{H' \times W' \times C'}$, where H' and W' are the dimensions of the feature map, and C' is the number of channels. Next, the discriminator applies a set of adaptive affine transformation matrices $A_1, A_2, \dots, A_n \in \mathbb{R}^{2 \times 3}$ to the feature map F , performing spatial transformations to generate n different local patches. For the j^{th} patch, the affine-transformed patch P_j is obtained using equation (5):

$$P_j = A_j F \quad (5)$$

where $P_j \in \mathbb{R}^{H_p \times W_p \times C'}$ represents the j^{th} patch, with H_p and W_p denoting the height and width of the patch, respectively, and C' being the number of channels in the feature map. Each generated patch P_j is fed into a small CNN for local authenticity evaluation, producing a scalar output $D(P_j) \in [0, 1]$. This scalar value represents the authenticity of the patch, where a value closer to 1 indicates a more realistic patch, while a value closer to 0 indicates a more synthetic or fake patch. The process of authenticity evaluation by the discriminator is described in equation (6):

$$D(P_j) = \sigma(\text{CNN}_{\text{patch}}(P_j)) \quad (6)$$

where σ is the sigmoid activation function, and $\text{CNN}_{\text{patch}}$ represents the discriminator network applied to each patch. To optimise the network's performance, a binary cross-entropy loss function is used to measure the authenticity of each patch between the generated and real images. The specific form is given in equation (7):

$$L_{\text{patch}} = \sum_{j=1}^n \left[\log(D(P_j^{\text{real}})) + \log(1 - D(P_j^{\text{fake}})) \right] \quad (7)$$

where P_j^{real} and P_j^{fake} represent the real and fake patches, respectively. The loss function trains the discriminator by maximising the authenticity of real patches while minimising the authenticity of fake patches.

Additionally, cloud occlusion often results in the loss of fine texture details, making the generated images appear overly smooth. To address this issue, this paper introduces a texture loss, with the specific process described in equation (8):

$$L_{\text{texture}} = \mathbb{E}_{x \sim p_{\text{data}}(x)} \left[\left\| \text{Texture}(G(x)) - \text{Texture}(x_{\text{cloud-free}}) \right\|_1 \right] \quad (8)$$

where $\text{Texture}(x)$ represents the texture features extracted using the Gabor filter, and $\|\cdot\|_1$ denotes the L_1 norm, which measures the texture difference between the generated and real images.

To ensure the global consistency of the generated images, we further introduce a global consistency loss L_{global} . This loss function optimises the restoration of the overall

structure in the generated image, ensuring consistency in the overall composition. The calculation process is given in equation (9):

$$L_{global} = \mathbb{E}_{x \sim p_{data}(x)} \left[\|G(x) - x_{cloud-free}\|_2 \right] \quad (9)$$

where $\|\cdot\|_2$ denotes the L_2 norm, which measures the difference between the generated and real images in terms of global structure.

Finally, the total loss function of the entire network integrates texture-aware loss, global consistency loss, and the loss from the APD. The specific expression of the total loss function is given in equation (10):

$$L_{final} = \alpha L_{texture} + \beta L_{global} + \gamma L_{patch} \quad (10)$$

where $L_{texture}$ represents the texture-aware loss, L_{global} is the global consistency loss, and L_{patch} is the loss computed by the APD. The coefficients α , β , and γ are the weighting factors for each loss term. By optimising this total loss function, the model can simultaneously enhance local detail restoration, cloud region reconstruction, and global structural consistency, thereby generating high-quality cloud-free images.

4 Experiment

4.1 Experimental setup and environment

This experiment was conducted on a computer equipped with an Intel Core i9-10900K processor, an NVIDIA GeForce RTX 3090 GPU, and 64GB of RAM. The operating system was Ubuntu 20.04 LTS, and the implementation was based on PyTorch 1.10.0 with Python 3.8. The model was trained using the Adam optimiser with an initial learning rate of 2×10^{-4} , a batch size of 16, and a total of 200 training epochs. The learning rate was decayed every ten epochs. MAGCN employed a three-layer GCN network, with each layer containing 1,536 feature channels. Additionally, the discriminator network adopted the APD, generating a total of 256 patches, each with a size of 32×32 pixels. The loss function combined texture loss $L_{texture}$, global consistency loss L_{global} , and adaptive patch loss L_{patch} , with weight coefficients of 0.5, 0.3 and 0.2, respectively, to balance detail restoration and global structure consistency.

4.2 Dataset and evaluation metrics

This experiment utilises four datasets: RICE1, RICE2, T-CLOUD, and WHUS2-CR. RICE1 and RICE2 are from the RICE dataset, where RICE1 is a thin cloud dataset containing 500 image pairs. The data is sourced from Google Earth, with an image size of 512×512 pixels, primarily focusing on thin cloud removal tasks. In contrast, RICE2 is a thick cloud dataset containing 736 image pairs, sourced from Landsat 8, with the same image size of 512×512 pixels. It is mainly used for handling thick cloud occlusion scenarios. To verify the generalisability of our algorithm, in addition to experiments on the RICE1 dataset, we also conducted experiments on RICE2 to evaluate the algorithm's performance in more complex cloud conditions. T-CLOUD is a thin cloud dataset acquired by the Landsat 8 satellite, consisting of 2,939 real image pairs. The time interval between image pairs is 16 days. The dataset is divided into a training set with 2,351 pairs

and a test set with 588 pairs, with an image size of 256×256 pixels. The distinctive characteristic of the T-CLOUD dataset is its long-time interval, which results in more complex cloud variations, making it suitable for studying cloud removal over extended time spans. WHUS2-CR is a dataset acquired by the Sentinel-2A satellite, using the satellite’s visible light bands to construct true-colour images. The time interval between image pairs corresponds to the satellite’s revisit period. WHUS2-CR is also a thin cloud dataset, containing 3,776 image pairs for training and 944 image pairs for testing, with an image size of 256×256 pixels.

For the evaluation metrics, we selected three commonly used image quality assessment standards: PSNR, SSIM, and NIQE. The calculation processes are shown in equations (11), (12) and (13), respectively.

$$PSNR = 10 \cdot \log_{10} \left(\frac{MAX_I^2}{MSE} \right) \quad (11)$$

$$SSIM(x, y) = \frac{(2\mu_x\mu_y + C_1)(2\sigma_{xy} + C_2)}{(\mu_x^2 + \mu_y^2 + C_1)(\sigma_x^2 + \sigma_y^2 + C_2)} \quad (12)$$

$$NIQE = \sqrt{(\mu_t - \mu_p)^T \left(\frac{\Sigma_t + \Sigma_p}{2} \right)^{-1} (\mu_t - \mu_p)} \quad (13)$$

Peak signal-to-noise ratio (PSNR) is used to measure the quality of image reconstruction, where a higher value indicates a greater similarity between the reconstructed image and the original image. Structural similarity index measure (SSIM) evaluates image quality based on structural similarity, with values closer to 1 indicating a higher structural resemblance between images. Natural image quality evaluator (NIQE) is a no-reference quality assessment method that measures the naturalness and visual quality of an image, where a lower value corresponds to better image quality. By using these three metrics, we can comprehensively evaluate our method’s performance in cloud removal from different perspectives.

4.3 Results and analysis

4.3.1 Ablation study

To further verify the contribution of each module to the performance of MAGC-GAN, we conducted an ablation study on the RICE2 and WHUS2-CR datasets. By progressively removing the multi-branch encoder, MAGCN, APD, and texture loss module, we analysed the impact of each component on image quality. A quantitative comparison was performed using PSNR, SSIM, and NIQE as evaluation metrics. The experimental results are shown in Table 1.

It can be observed that MAGC-GAN achieves the best performance on the RICE2 dataset, with a PSNR of 38.26, SSIM of 0.94, and NIQE of 3.12. The removal of any module leads to varying degrees of decline in these metrics. In particular, after removing the MAGCN module, PSNR drops to 34.98, SSIM decreases to 0.89, and NIQE rises to 3.50, indicating that MAGCN plays a crucial role in capturing image structures and details. Similarly, removing the multi-branch encoder results in a decrease in PSNR to 36.15 and SSIM to 0.91, while NIQE increases to 3.35, demonstrating its importance in

handling complex image details and multi-scale information. After removing the APD module, PSNR drops to 35.76, SSIM to 0.90, and NIQE rises to 3.45. Although the overall performance remains relatively good, there is a noticeable decline in image contrast and detail restoration. Removing the texture loss module results in PSNR of 36.45, SSIM of 0.92, and NIQE of 3.30. While the performance is still competitive, the naturalness of the image and preservation of texture details are significantly affected.

Table 1 Impact of each module in MAGC-GAN on model performance

Methods	RICE2			WHUS2-CR		
	PSNR	SSIM	NIQE	PSNR	SSIM	NIQE
w/o multi-branch encoder	36.15	0.91	3.35	30.85	0.88	4.05
w/o MAGCN	34.98	0.89	3.50	29.67	0.85	4.18
w/o APD	35.76	0.90	3.45	30.10	0.87	4.12
w/o texture loss	36.45	0.92	3.30	31.50	0.89	4.00
MAGC-GAN	38.26	0.94	3.12	32.67	0.93	3.76

On the WHUS2-CR dataset, MAGC-GAN achieves a PSNR of 32.67, SSIM of 0.93, and NIQE of 3.76, still outperforming the models with removed modules. After removing the MAGCN module, PSNR drops to 29.67, SSIM decreases to 0.85, and NIQE rises to 4.18, showing a significant change. This highlights MAGCN’s critical role in restoring image details and structures in this dataset. The removal of the multi-branch encoder also leads to a decline in PSNR and SSIM, though the impact is less pronounced compared to removing MAGCN, yet still not negligible for image quality. Removing APD results in a significant drop in PSNR and SSIM, reflecting the importance of APD in enhancing image contrast and colour restoration. After removing texture loss, the PSNR is 31.50, SSIM is 0.89, and NIQE is 4.00, leading to slight losses in image details and naturalness.

4.3.2 Comparison experiments

To verify the advantages of MAGCN, we compare it with several commonly used graph neural network methods, including GCN (Kipf and Welling, 2016), GNN (Scarselli et al., 2008), and GAT (Velickovic et al., 2017). Experiments were conducted on the RICE2 and WHUS2-CR datasets, and the results are shown in Table 2.

Table 2 Performance comparison between the proposed MAGCN and other graph neural network methods

Methods	RICE2			WHUS2-CR		
	PSNR	SSIM	NIQE	PSNR	SSIM	NIQE
GNN	35.65	0.91	3.36	31.35	0.89	3.91
GCN	34.12	0.89	3.47	30.45	0.86	4.01
GAT	36.08	0.92	3.25	31.85	0.90	3.83
MAGCN	38.26	0.94	3.12	32.67	0.93	3.76

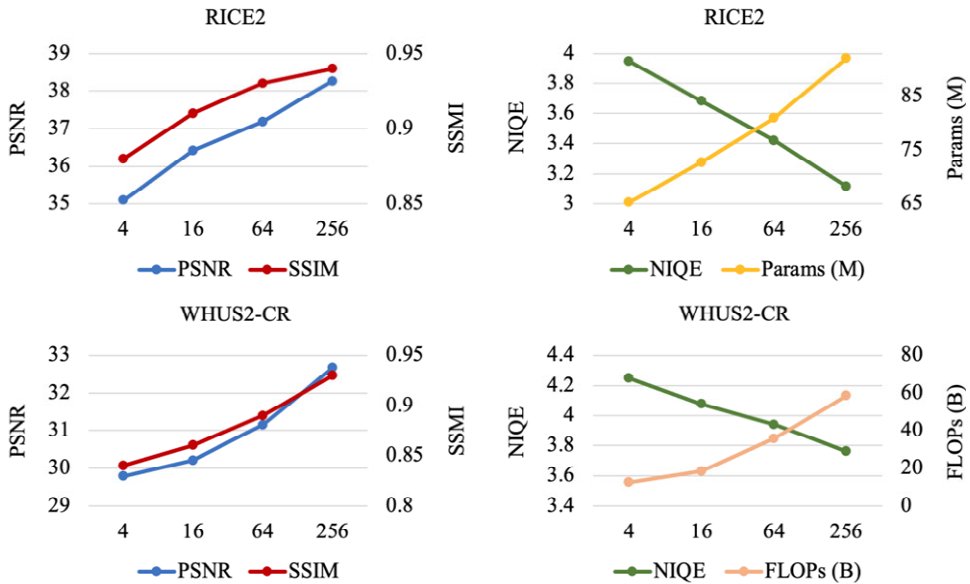
From the experimental results, it can be observed that MAGCN achieves the best performance on both the RICE2 and WHUS2-CR datasets, significantly outperforming other methods in terms of PSNR, SSIM, and NIQE. On the RICE2 dataset, MAGCN

surpasses GCN, GNN, and GAT in all metrics, with the lowest NIQE value, indicating that it can restore more details and structural information while maintaining the most natural appearance of the images. In contrast, GCN exhibits weaker performance, with PSNR and SSIM values significantly lower than those of other methods, and a higher NIQE value, reflecting its limitations in cloud structure modelling and detail restoration. On the WHUS2-CR dataset, MAGCN maintains its superiority, achieving a PSNR of 32.67, SSIM of 0.93, and NIQE of 3.76, all of which remain the highest among the compared methods. Although GNN and GAT show some improvements, with PSNR values of 31.35 and 31.85, respectively, they still fall short of MAGCN. Moreover, their NIQE values are higher than that of MAGCN, indicating that they are less effective in detail recovery and preserving the natural appearance of images. Overall, MAGCN, with its innovative graph convolution mechanism and multi-scale feature fusion, demonstrates clear advantages over GCN, GNN, and GAT in terms of detail restoration and the naturalness of image reconstruction. In particular, in complex cloud occlusion scenarios, MAGCN better captures global dependencies, thereby enhancing the visual quality and realism of the generated images.

4.3.3 Hyperparameter experiment

To further verify the performance of the APD, we conducted experiments with different numbers of patches, specifically using 4, 16, 64, and 256 patches. The performance of the model under different patch numbers was compared on the RICE2 and WHUS2-CR datasets, and the experimental results are shown in Figure 3.

Figure 3 Impact of different patch numbers in the APD module on model performance (see online version for colours)



It can be observed that as the number of patches increases, the model's performance improves significantly. On the RICE2 dataset, when the number of patches is only 4, PSNR is 35.10, SSIM is 0.88, and NIQE is relatively high at 3.95. This indicates that

with too few patches, the model fails to fully capture local image details, resulting in poor cloud removal performance, blurry cloud edges, and detail loss. A similar trend can be observed on the WHUS2-CR dataset, where with only four patches, PSNR is 29.78, SSIM is 0.84, and NIQE is as high as 4.25. This suggests that at higher resolutions, a small number of patches cannot ensure the naturalness and consistency of image reconstruction. When the number of patches increases to 16, PSNR and SSIM improve moderately, while NIQE decreases, indicating that more patches allow the model to focus more precisely on local textures and contrast. However, certain limitations remain. With 64 patches, the performance improves further, particularly in SSIM and NIQE, demonstrating that the model can better restore details in cloud-covered regions, producing images that more closely resemble real ground textures. When the number of patches is further increased to 256, the model achieves its best performance on both the RICE2 and WHUS2-CR datasets, with PSNR values of 38.26 and 32.67, SSIM values of 0.94 and 0.93, and NIQE values dropping to 3.12 and 3.76, respectively. This indicates that using 256 patches allows the model to fully leverage local discrimination information, enhancing the detail quality in cloud-removed areas while maintaining overall image consistency. However, although increasing the number of patches improves model performance, it also significantly increases computational cost. The number of parameters grows from 65.32 M at four patches to 92.10 M at 256 patches, while FLOPs increase from 12.50 G to 58.75 G, indicating that computational complexity increases exponentially with the number of patches. Therefore, in practical applications, the choice of patch number should balance computational resources and model performance. When computational resources are limited, 256 patches may be a more cost-effective choice, providing high image quality while controlling computational cost.

4.3.4 SOTA comparison experiment

To comprehensively evaluate the performance of MAGC-GAN, we compared it with state-of-the-art (SOTA) cloud removal methods across four datasets. The comparison results on RICE1 and RICE2 datasets are shown in Table 3, while the results on T-CLOUD and WHUS2-CR datasets are also presented in Table 3.

Experimental results show that MAGC-GAN achieves consistently superior performance on both the RICE1 and RICE2 remote sensing datasets. Its PSNR and SSIM scores are significantly higher than those of existing methods, while its NIQE is the lowest among all, indicating that the images generated by MAGC-GAN are visually closer to real cloud-free images and exhibit a more natural and realistic appearance overall.

In comparison with mainstream methods, MS-GAN demonstrates strong performance on the RICE1 dataset, achieving a PSNR of 32.50 and an SSIM of 0.93, validating the effectiveness of its multi-scale generation architecture for detail restoration. However, on the more challenging RICE2 dataset, MS-GAN's NIQE rises to 5.31, suggesting that it still produces noticeable artefacts when dealing with thick cloud occlusion, and struggles to accurately reconstruct ground objects, thereby limiting the overall image quality.

Another method, RCAN, also shows some advantage in SSIM, but its PSNR scores are only 26.68 on RICE1 and 19.39 on RICE2 – both considerably lower than those of MAGC-GAN. This indicates that although RCAN utilises a residual channel attention mechanism to enhance feature extraction in cloud-covered regions, its ability to reconstruct information under complex cloud conditions remains limited, especially in

thick cloud areas where the reconstruction quality is poor and the overall image fidelity is low.

Table 3 Quantitative comparison of different SOTA cloud removal methods on the RICE1 and RICE2 datasets

<i>Methods</i>	<i>RICE1</i>			<i>RICE2</i>		
	<i>PSNR</i>	<i>SSIM</i>	<i>NIQE</i>	<i>PSNR</i>	<i>SSIM</i>	<i>NIQE</i>
DCP (He et al., 2010)	18.79	0.76	4.83	16.99	0.64	4.82
SPA-GAN (Pan, 2020)	29.60	0.91	4.91	30.93	0.87	5.03
YUV-GAN (Wen et al., 2021)	23.45	0.88	5.22	18.23	0.81	7.29
MS-GAN (Xu et al., 2021)	32.50	0.93	3.87	32.34	0.88	5.31
RCAN (Wen et al., 2022)	26.68	0.93	4.27	19.39	0.84	3.87
CVAE (Ding et al., 2022)	33.05	0.88	5.63	35.54	0.91	5.52
CMNet (Liu et al., 2024b)	37.59	0.96	4.19	37.56	0.92	5.21
Patch-GAN (Ma et al., 2025)	35.72	0.94	3.96	36.11	0.91	3.48
SRG-GAN (Yang et al., 2024)	36.38	0.95	3.88	36.67	0.92	3.29
Cloudformer-CycleGAN (Fang, 2024)	36.91	0.95	3.65	37.23	0.93	3.22
MAGC-GAN	<i>38.34</i>	<i>0.97</i>	<i>3.36</i>	<i>38.26</i>	<i>0.94</i>	<i>3.12</i>

In contrast, MAGC-GAN achieves a significant breakthrough in modelling spatial dependencies within images. Its introduction of the MAGCN not only overcomes the limitations of traditional CNNs constrained by local receptive fields, but also outperforms existing GCN-based approaches through dynamic graph modelling and multi-scale feature integration. MAGCN captures both fine-grained local details and global structural information across multiple scales and fuses them using adaptive weighting, enabling more accurate cloud structure modelling and ground object restoration – particularly effective in scenes with thick cloud cover.

Unlike MS-GAN, which relies on synthetic cloud generation strategies for training, MAGC-GAN directly learns cloud removal features from real remote sensing data, avoiding potential domain bias and enhancing generalisation and restoration quality in real-world scenarios. Moreover, the APD adopted in MAGC-GAN addresses the shortcomings of RCAN, which relies solely on global information. By combining global structural optimisation with localised cloud-edge refinement, APD significantly improves detail restoration in heavily cloud-covered areas, enhancing both the realism and structural consistency of the generated images.

Experimental results demonstrate that MAGC-GAN outperforms existing mainstream methods on both the T-CLOUD and WHUS2-CR remote sensing cloud removal datasets. It achieves the highest scores in PSNR and SSIM, while also delivering the best performance in NIQE evaluation. These results indicate that the cloud-free images generated by MAGC-GAN surpass other methods in detail preservation, structural reconstruction, and visual naturalness, resulting in superior overall image quality.

Among the compared methods, CMNet achieves SSIM scores close to those of MAGC-GAN, suggesting that its use of the Swin Transformer architecture is effective in modelling global information and enhancing cloud removal. However, CMNet falls slightly behind MAGC-GAN in terms of PSNR and NIQE, indicating that its generated

images still contain blurry regions – especially in thick cloud-covered areas – where it fails to fully recover the details of occluded ground objects.

Table 4 Quantitative comparison of different SOTA cloud removal methods on the T-CLOUD and WHUS2-CR datasets

<i>Methods</i>	<i>T-CLOUD</i>			<i>WHUS2-CR</i>		
	<i>PSNR</i>	<i>SSIM</i>	<i>NIQE</i>	<i>PSNR</i>	<i>SSIM</i>	<i>NIQE</i>
DCP (He et al., 2010)	17.55	0.67	7.37	15.08	0.59	5.44
SPA-GAN (Pan, 2020)	27.41	0.82	5.37	027.72	0.83	5.83
YUV-GAN (Wen et al., 2021)	22.91	0.81	6.06	17.75	0.76	5.72
MS-GAN (Xu et al., 2021)	28.05	0.83	4.93	22.63	0.77	5.18
RCAN (Wen et al., 2022)	25.06	0.86	4.99	21.36	0.75	5.38
CVAE (Ding et al., 2022)	29.67	0.89	4.91	29.50	0.85	5.82
CMNet (Liu et al., 2024b)	31.89	0.90	4.94	30.84	0.90	4.81
Patch-GAN (Ma et al., 2025)	31.35	0.91	4.52	30.65	0.89	4.05
SRG-GAN (Yang et al., 2024)	32.04	0.92	4.31	31.15	0.91	3.91
Cloudformer-CycleGAN (Fang, 2024)	32.77	0.92	4.15	32.05	0.92	3.83
MAGC-GAN	33.48	0.93	3.83	32.67	0.93	3.76

The CVAE method utilises a conditional variational autoencoder to generate multiple candidate cloud-free images for improved accuracy. However, its NIQE score on the WHUS2-CR dataset reaches 5.82, revealing the presence of noticeable artefacts that compromise visual quality. This is particularly evident in complex cloud conditions, where the single encoder-decoder architecture of CVAE struggles to balance global structural consistency with local detail reconstruction.

In contrast, MAGC-GAN demonstrates significant advantages in restoring regions affected by thick cloud coverage. Although CMNet incorporates a local information memory module (LIMM) and a global information assistance module (GIAM), it still relies primarily on the transformer structure for global modelling. This results in limited performance in accurately recovering cloud boundaries, thus constraining further improvement in PSNR. MAGC-GAN addresses this issue by introducing the MAGCN, which models pixel relationships across multiple scales. Through graph-based spatial modelling, MAGCN enhances the recognition and reconstruction of cloud-covered regions, achieving a balance between global consistency and local detail restoration.

Furthermore, the APD in MAGC-GAN further improves the precision of local detail recovery, particularly in heavily clouded regions. Unlike CVAE, which depends on a single network to generate cloud-free images, MAGC-GAN incorporates multi-scale feature fusion and edge-aware weighting strategies. These mechanisms enable the network to effectively model and restore clouds of varying thickness and complexity, ultimately producing clearer, more natural, and higher-quality cloud-free images.

Finally, to evaluate the computational complexity of the proposed algorithm and explore its feasibility for real-world deployment, we further compared the performance of mainstream methods in terms of both time and space complexity. Specifically, we considered three key indicators: the number of model parameters (Params), the number of floating-point operations (FLOPs), and the inference speed (FPS). The comparison results are presented in Table 5.

Table 5 Comprehensive comparison including parameters, FLOPs, and inference speed

<i>Methods</i>	<i>Params (M)</i>	<i>FLOPs (G)</i>	<i>FPS</i>
DCP (He et al., 2010)	1.2	3.8	62.3
SPA-GAN (Pan, 2020)	17.6	45.2	22.1
YUV-GAN (Wen et al., 2021)	12.9	39.5	26.4
MS-GAN (Xu et al., 2021)	25.7	68.9	18.3
RCAN (Wen et al., 2022)	15.3	51.4	20.5
CVAE (Ding et al., 2022)	34.2	74.8	14.8
CMNet (Liu et al., 2024b)	42.1	82.5	16.0
Patch-GAN (Ma et al., 2025)	35.5	60.2	20.3
SRG-GAN (Yang et al., 2024)	36.8	63.9	18.7
Cloudformer-CycleGAN (Fang, 2024)	37.2	66.1	18.1
MAGC-GAN	39.4	58.7	19.6

As shown in Table 5, MAGC-GAN achieves the best overall trade-off between performance and efficiency. While maintaining a moderate model size (39.4M parameters) and lower computational complexity than some recent methods like CVAE or CMNet, it delivers the highest PSNR (33.48), SSIM (0.93), and the lowest NIQE (3.83). Its inference speed of 19.6 FPS is also competitive, making it suitable for practical deployment scenarios. These results confirm that MAGC-GAN achieves SOTA cloud removal performance with superior balance in quality, complexity, and efficiency.

4.3.5 Visualisation experiment

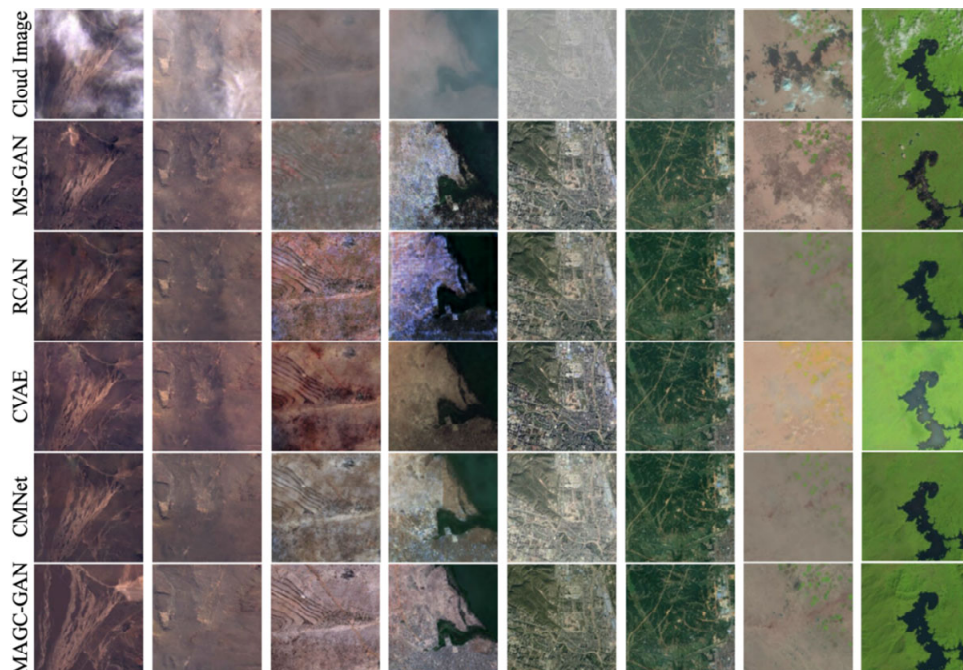
To further verify the effectiveness of MAGC-GAN in cloud removal tasks, we conducted a visualisation experiment by selecting cloud-removed images from four datasets and comparing them with the cloud removal results of other SOTA methods, as shown in Figure 4.

From the visualisation experiment results, MAGC-GAN demonstrates a clear advantage in cloud removal tasks. Compared to other SOTA methods, MAGC-GAN can better restore ground object information obscured by clouds while preserving rich details and natural colours. Specifically, in terms of cloud removal effectiveness, MS-GAN, RCAN, and CVAE can reduce cloud interference to some extent, but they still suffer from varying degrees of information loss and blurring in thick cloud areas. MS-GAN relies on synthetic data for training, which enables good recovery in thin cloud regions but results in noticeable distortion and detail loss in thick cloud areas. RCAN employs a channel attention mechanism to enhance feature representation; however, it tends to introduce excessive smoothing during cloud removal, leading to the loss of fine details. Additionally, CVAE generates multiple possible cloud-free images, but its results often lack sharpness, causing blurred texture details. CMNet, one of the stronger-performing methods, effectively restores ground structure information and performs better in preserving local details than the previously mentioned methods. However, since it uses a cascaded memory network, it still struggles in extreme thick cloud regions, where unnatural edge transitions or partial detail loss may occur.

In contrast, MAGC-GAN achieves a more comprehensive restoration of ground objects, depicting cloud-covered details more naturally while avoiding excessive

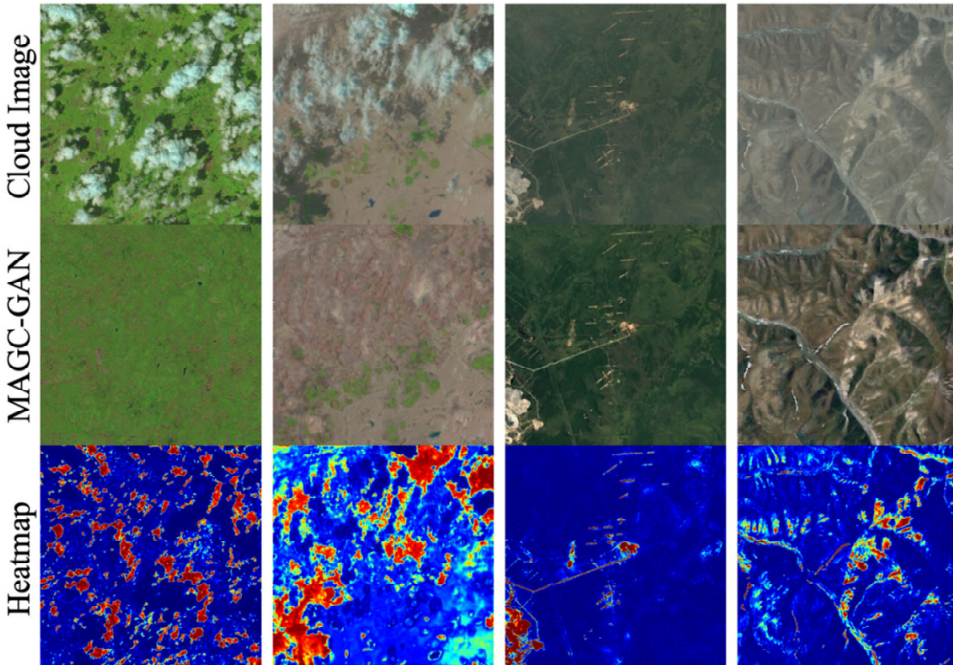
smoothing and edge blurring issues. The adaptive graph convolution mechanism in MAGCN effectively enhances spatial information modelling, making the cloud-removed image structure more coherent. Meanwhile, APD strengthens local discrimination, improving detail restoration and ensuring that the cloud-free image retains rich high-frequency information and natural textures.

Figure 4 Qualitative comparison of different methods across multiple datasets (see online version for colours)



Additionally, to further analyse the attention distribution of MAGC-GAN during image processing, we applied heatmap visualisation to intuitively display the areas focused on during cloud removal. The results are shown in Figure 5.

From the heatmap visualisation experiment, it can be observed that MAGC-GAN effectively focuses on cloud-covered areas during the cloud removal process and accurately restores key ground object information. The heatmap illustrates the model's attention distribution in the cloud removal task, where red and yellow areas indicate regions with high attention, while blue areas represent regions with low attention. The results show that MAGC-GAN primarily concentrates on severely cloud-covered areas, particularly along cloud edges, where it exhibits a stronger response. This indicates that MAGCN, through adaptive graph convolution operations, effectively enhances the modelling capability for complex cloud structures, enabling the network to accurately locate cloud-covered areas and utilise surrounding information for better restoration.

Figure 5 Heatmap visualisation of intermediate feature maps in MAGC-GAN (see online version for colours)

5 Conclusions

Thick cloud occlusion significantly affects the quality and application of optical remote sensing images. To address this issue, this paper proposes the MAGC-GAN, which integrates the MAGCN to enhance global modelling capability and employs the APD to refine local detail restoration. Experimental results demonstrate that MAGC-GAN outperforms existing methods across multiple datasets, achieving the best performance in PSNR, SSIM, and NIQE, while also demonstrating advantages in thick cloud removal, edge detail recovery, and visual consistency. Ablation experiments and heatmap visualisations further verify the effectiveness of MAGCN and APD in improving cloud removal quality. Despite its excellent performance in thick cloud removal tasks, MAGC-GAN still has some limitations. When dealing with extremely complex cloud structures, the model may still suffer from detail loss or reconstruction bias, and its computational complexity remains relatively high. Future work will focus on optimising the lightweight design of the model, exploring more efficient graph convolution structures and attention mechanisms, and integrating multi-source remote sensing data to further enhance the model's stability and generalisation ability, making it more suitable for large-scale remote sensing applications.

Declarations

All authors declare that they have no conflicts of interest.

Data availability statement

The datasets used and analysed during the current study available from the corresponding author on reasonable request.

References

- Baskar, D., Parambalath, N.K. and Krishnanunni, S.O. (2024) ‘Variational mode decomposition-enhanced thin cloud removal using UNet vision transformer cycle-consistent generative adversarial network’, *Journal of Applied Remote Sensing*, Vol. 18, No. 2, pp.26504–26504.
- Bie, Q. and Su, X. (2024) ‘MCGFE-CR: cloud removal with multiscale context-guided feature enhancement network’, *IEEE Access*, Vol. 12, pp.181303–181315, DOI: 10.1109/ACCESS.2024.3491171..
- Ding, H., Zi, Y. and Xie, F. (2022) ‘Uncertainty-based thin cloud removal network via conditional variational autoencoders’, in *Proceedings of the Asian Conference on Computer Vision*, pp.469–485.
- Dou, A., Hao, Y., Liu, W., Li, L., Wang, Z. and Liu, B. (2024) ‘Remote sensing image cloud removal based on multi-scale spatial information perception’, *Multimedia Systems*, Vol. 30, No. 5, p.249.
- Ebel, P., Garnot, V.S.F., Schmitt, M., Wegner, J.D. and Zhu, X.X. (2023) ‘UnCRtainTS: uncertainty quantification for cloud removal in optical satellite time series’, in *Proceedings of the IEEE/CVF Conference on Computer Vision and Pattern Recognition*, pp.2086–2096.
- Fang, Y. (2024) ‘Cloudformer-CycleGAN: an efficient cloud removal network integrating residual learning and channel spatial attention mechanism’, in *Journal of Physics: Conference Series*, IOP Publishing, Vol. 2863, No. 1, p.12035.
- Han, J., Zhou, Y., Gao, X. and Zhao, Y. (2024) ‘Thin cloud removal generative adversarial network based on sparse transformer in remote sensing images’, *Remote Sensing*, Vol. 16, No. 19, p.3658.
- Hao, Y., Jiang, W., Liu, W., Li, Y. and Liu, B.D. (2023) ‘Selecting information fusion generative adversarial network for remote-sensing image cloud removal’, *IEEE Geoscience and Remote Sensing Letters*, Vol. 20, pp.1–5, DOI: 10.1109/LGRS.2023.3296517.
- He, K., Sun, J. and Tang, X. (2010) ‘Single image haze removal using dark channel prior’, *IEEE Transactions on Pattern Analysis and Machine Intelligence*, Vol. 33, No. 12, pp.2341–2353.
- Ji, Z. and Zhong, X. (2024) ‘Bidirectional attention network for real-time segmentation of forest fires based on UAV images’, *International Journal of Information and Communication Technology*, Vol. 25, No. 6, pp.38–51.
- Jin, M., Wang, P. and Li, Y. (2024) ‘HYA-GAN: remote sensing image cloud removal based on hybrid attention generation adversarial network’, *International Journal of Remote Sensing*, Vol. 45, No. 6, pp.1755–1773.
- Jing, R., Duan, F., Lu, F., Zhang, M. and Zhao, W. (2023) ‘Denoising diffusion probabilistic feature-based network for cloud removal in Sentinel-2 imagery’, *Remote Sensing*, Vol. 15, No. 9, p.2217.
- Kipf, T.N. and Welling, M. (2016) *Semi-Supervised Classification with Graph Convolutional Networks*, arXiv preprint arXiv:1609.02907.

- Li, A., Guan, G., Zhao, H., Li, S., Zhu, J., Han, X., Wang, Y. and Pan, J. (2024a) 'Integrated methodology for atmospheric correction and cloud removal of multispectral remote sensing images using guided diffusion model', *IEEE Transactions on Geoscience and Remote Sensing*, Vol. 62, pp.1–21, DOI: 10.1109/TGRS.2024.3497180.
- Li, X., Zhao, X., Wang, F. and Ren, P. (2024b) 'HF-T2CR: high-fidelity thin and thick cloud removal in optical satellite images through SAR fusion', *IEEE Transactions on Geoscience and Remote Sensing*, Vol. 62, pp.1–13, DOI: 10.1109/TGRS.2024.3416128.
- Li, C., Liu, X. and Li, S. (2023a) 'Transformer meets GAN: cloud-free multispectral image reconstruction via multisensor data fusion in satellite images', *IEEE Transactions on Geoscience and Remote Sensing*, Vol. 61, pp.1–13, DOI: 10.1109/TGRS.2023.3326545.
- Li, J., Shi, P., Hu, Q. and Zhang, Y. (2023b) 'QGORe: quadratic-time guaranteed outlier removal for point cloud registration', *IEEE Transactions on Pattern Analysis and Machine Intelligence*, Vol. 45, No. 9, pp.11136–11151.
- Liu, G., Shan, Z., Meng, Y., Akbar, T.A. and Ye, S. (2024a) 'RDPGNet: a road extraction network with dual-view information perception based on GCN', *Journal of King Saud University – Computer and Information Sciences*, Vol. 36, No. 3, p.102009.
- Liu, J., Pan, B. and Shi, Z. (2024b) 'Cascaded memory network for optical remote sensing imagery cloud removal', *IEEE Transactions on Geoscience and Remote Sensing*, Vol. 62, pp.1–11, DOI: 10.1109/TGRS.2024.3376609.
- Liu, K., Xia, L. and Xu, J. (2023a) 'An information management system of land resources based on UAV remote sensing', *International Journal of Information and Communication Technology*, Vol. 23, No. 2, pp.107–125.
- Liu, Z., Zhao, Y., Zhan, S., Liu, Y., Chen, R. and He, Y. (2023b) 'PCDNF: revisiting learning-based point cloud denoising via joint normal filtering', *IEEE Transactions on Visualization and Computer Graphics*.
- Lu, Y., Zhao, Y., Yang, M., Zhao, Y., Huang, L. and Cui, B. (2024) 'BI2Net: graph-based boundary-interior interaction network for raft aquaculture area extraction from remote sensing images', *IEEE Geoscience and Remote Sensing Letters*, Vol. 21, pp.1–5, DOI: 10.1109/LGRS.2024.3369721.
- Ma, W., Karakus, O. and Rosin, P.L. (2025) *Patch-GAN Transfer Learning with Reconstructive Models for Cloud Removal*, arXiv preprint arXiv:2501.05265.
- Ma, X., Huang, Y., Zhang, X., Pun, M.O. and Huang, B. (2023) 'Cloud-EGAN: rethinking CycleGAN from a feature enhancement perspective for cloud removal by combining CNN and transformer', *IEEE Journal of Selected Topics in Applied Earth Observations and Remote Sensing*, Vol. 16, pp.4999–5012, DOI: 10.1109/JSTARS.2023.3280947.
- Pan, H. (2020) *Cloud Removal for Remote Sensing Imagery via Spatial Attention Generative Adversarial Network*, arXiv preprint arXiv:2009.13015.
- Scarselli, F., Gori, M., Tsoi, A.C., Hagenbuchner, M. and Monfardini, G. (2008) 'The graph neural network model', *IEEE Transactions on Neural Networks*, Vol. 20, No. 1, pp.61–80.
- Song, X., Hua, Z. and Li, J. (2024) 'Context spatial awareness remote sensing image change detection network based on graph and convolution interaction', *IEEE Transactions on Geoscience and Remote Sensing*, Vol. 62, pp.1–16, DOI: 10.1109/TGRS.2024.3357524.
- Velickovic, P., Cucurull, G., Casanova, A., Romero, A., Lio, P. and Bengio, Y. (2017) 'Graph attention networks', *Stat.*, Vol. 1050, No. 20, pp.10–48550.
- Wang, M., Song, Y., Wei, P., Xian, X., Shi, Y. and Lin, L. (2024a) 'IDF-CR: iterative diffusion process for divide-and-conquer cloud removal in remote-sensing images', *IEEE Transactions on Geoscience and Remote Sensing*, Vol. 62, pp.1–14, DOI: 10.1109/TGRS.2024.3378720.
- Wang, W., Liu, C., Liu, G. and Wang, X. (2024b) 'CF-GCN: graph convolutional network for change detection in remote sensing images', *IEEE Transactions on Geoscience and Remote Sensing*, Vol. 62, pp.1–13, DOI: 10.1109/TGRS.2024.3357085.
- Wen, X., Pan, Z., Hu, Y. and Liu, J. (2021) 'Generative adversarial learning in YUV color space for thin cloud removal on satellite imagery', *Remote Sensing*, Vol. 13, No. 6, p.1079.

- Wen, X., Pan, Z., Hu, Y. and Liu, J. (2022) 'An effective network integrating residual learning and channel attention mechanism for thin cloud removal', *IEEE Geoscience and Remote Sensing Letters*, Vol. 19, pp.1–5, DOI: 10.1109/LGRS.2022.3161062.
- Xiao, Y. (2024) 'Removal of thin clouds from high-resolution optical images based on multiscale feature fusion', in *International Conference on Advanced Image Processing Technology (AIPT 2024)*, SPIE, Vol. 13257.
- Xu, Z., Wu, K., Huang, L., Wang, Q. and Ren, P. (2021) 'Cloudy image arithmetic: a cloudy scene synthesis paradigm with an application to deep-learning-based thin cloud removal', *IEEE Transactions on Geoscience and Remote Sensing*, Vol. 60, pp.1–16, DOI: 10.1109/TGRS.2021.3122253.
- Yang, J., Wang, W., Chen, K., Liu, L., Zou, Z. and Shi, Z. (2024) 'Structural representation-guided GAN for remote sensing image cloud removal', *IEEE Geoscience and Remote Sensing Letters*, Vol. 22, pp.1–5, DOI: 10.1109/LGRS.2024.3516078.
- Zhang, S., Li, X., Zhou, X., Wang, Y. and Hu, Y. (2023) 'Cloud removal using SAR and optical images via attention mechanism-based GAN', *Pattern Recognition Letters*, Vol. 175, pp.8–15, <https://doi.org/10.1016/j.patrec.2023.09.014>.
- Zhang, Y., Ming, D., Dong, D. and Xu, L. (2024) 'Object-oriented U-GCN for open-pit mining extraction from high spatial resolution remote-sensing images of complex scenes', *International Journal of Remote Sensing*, Vol. 45, No. 22, pp.8313–8333.
- Zhao, M., Olsen, P. and Chandra, R. (2023) 'Seeing through clouds in satellite images', *IEEE Transactions on Geoscience and Remote Sensing*, Vol. 61, pp.1–16, DOI: 10.1109/TGRS.2023.3239592.
- Zhao, X. and Jia, K. (2023) 'Cloud removal in remote sensing using sequential-based diffusion models', *Remote Sensing*, Vol. 15, No. 11, p.2861.
- Zheng, W.J., Zhao, X.L., Zheng, Y.B., Lin, J., Zhuang, L. and Huang, T.Z. (2023) 'Spatial-spectral-temporal connective tensor network decomposition for thick cloud removal', *ISPRS Journal of Photogrammetry and Remote Sensing*, Vol. 199, pp.182–194, <https://doi.org/10.1016/j.isprsjprs.2023.04.006>.
- Zhou, W., Huang, S., Luo, Q. and Yu, L. (2024a) 'Research on a ship target detection method in remote sensing images at sea', *International Journal of Information and Communication Technology*, Vol. 25, No. 12, pp.29–45.
- Zhou, H., Wang, Y., Liu, W., Tao, D., Ma, W. and Liu, B. (2024b) 'MSC-GAN: a multi-stream complementary generative adversarial network with grouping learning for multitemporal cloud removal', *IEEE Transactions on Geoscience and Remote Sensing*, Vol. 63, pp.1–17, DOI: 10.1109/TGRS.2024.3507214.
- Zhou, Y., Jing, W., Wang, J., Chen, G., Scherer, R. and Damaševičius, R. (2022) 'MSAR-DefogNet: lightweight cloud removal network for high resolution remote sensing images based on multi scale convolution', *IET Image Processing*, Vol. 16, No. 3, pp.659–668.
- Zi, Y., Ding, H., Xie, F., Jiang, Z. and Song, X. (2023) 'Wavelet integrated convolutional neural network for thin cloud removal in remote sensing images', *Remote Sensing*, Vol. 15, No. 3, p.781.